THE ASTROPHYSICAL JOURNAL, 379:245–259, 1991 September 20

THE ANALYSIS OF APPARENT OPTICAL DEPTH PROFILES FOR INTERSTELLAR ABSORPTION LINES

BLAIR D. SAVAGE AND KENNETH R. SEMBACH
Washburn Observatory, University of Wisconsin, 475 N. Charter Street, Madison, WI 53706
Received 1991 February 8; accepted 1991 April 8

ABSTRACT

The *apparent optical depth method*, a procedure for analyzing interstellar absorption lines, is discussed. The method involves converting observed absorption-line profiles into profiles of apparent optical depth, $\tau_a(v)$, and apparent column density per unit velocity, $N_a(v)$. By comparing $N_a(v)$ profiles for a given interstellar species having two or more absorption lines which differ in the product $f\lambda$, it is possible to directly infer the presence or absence of unresolved saturated structure in the profiles. The method is illustrated using interstellar absorption-line data from the *IUE* satellite for the highly ionized gas toward HD 64760. Additional illustrations and a study of the accuracy of the method are provided through a series of numerical simulations of multicomponent interstellar absorption situations. The method is compared to the standard curve of growth method for deriving interstellar column densities. The principal value of the apparent optical depth method is that the absorption-line data are directly converted into a form (i.e., plots of column density per unit velocity) that provides for direct scientific interpretations of the physical conditions in the interstellar absorbing medium as a function of velocity.

Subject headings: interstellar matter — line profiles — ultraviolet: spectra

1. INTRODUCTION

An interstellar absorption line having optical depth, $\tau(\lambda)$, as a function of wavelength, λ, will appear in the spectrum of a star according to

$$I(\lambda) = I_0(\lambda) \exp[-\tau(\lambda)] , \quad (1)$$

where $I(\lambda)$ and $I_0(\lambda)$ are the intensities with and without the absorption, respectively. When such an absorption is recorded with an instrument having a finite resolution defined by its instrumental spectral spread function, $\phi_I(\Delta\lambda)$, the recorded spectrum is a convolution of the intrinsic spectrum and the spread function,

$$I_{\rm obs}(\lambda) = \{I_0(\lambda) \exp[-\tau(\lambda)]\} \otimes \phi_I(\Delta\lambda) . \quad (2)$$

Usually the intensity of the stellar spectrum, $I_0(\lambda)$, changes slowly over the width of the spread function, and equation (2) simply becomes

$$I_{\rm obs}(\lambda) = I_0(\lambda)\{\exp[-\tau(\lambda)] \otimes \phi_I(\Delta\lambda)\} . \quad (3)$$

From equations (1) and (3) we define two kinds of optical depth,

$$\tau(\lambda) = \ln[I_0(\lambda)/I(\lambda)] , \quad (4)$$

and

$$\tau_a(\lambda) = \ln[I_0(\lambda)/I_{\rm obs}(\lambda)] . \quad (5)$$

The optical depth, $\tau(\lambda)$, obtained from equation (4) is the *true* optical depth as determined from the true line profile. The optical depth, $\tau_a(\lambda)$, obtained from equation (5) is hereafter referred to as the *apparent* optical depth. The apparent optical depth is an instrumentally blurred version of the true optical depth. However, the instrumental blurring occurs in intensity space according to equation (3), and therefore the apparent optical depth is given by

$$\tau_a(\lambda) = \ln [\![1/\{\exp[-\tau(\lambda)] \otimes \phi_I(\Delta\lambda)\}]\!] . \quad (6)$$

For $\tau(\lambda) \ll 1$, note that $\tau_a(\lambda) = \tau(\lambda) \otimes \phi_I(\Delta\lambda)$. If the instrumental resolution is very high compared to the line width (i.e., FWHM[line] $\gg$ FWHM[ϕ_I], where FWHM[line] and FWHM[ϕ_I] refer to the full widths at half-maximum intensity of the absorption line and instrumental spread function, respectively), then $\tau_a(\lambda)$ will be a good representation of $\tau(\lambda)$ provided the measurements have high signal to noise and the continuum level is well defined. Note that large values of $\tau(\lambda)$ are difficult to measure because there will usually be large relative uncertainties in the measured intensity for small values of that intensity. This occurs, for example, in the cores of strong absorption lines.

Currently, the most common techniques used for deriving column densities from absorption-line measurements are:

1.—The curve of growth method which relates the observed absorption-line equivalent width, W_λ, and the product $Nf\lambda$, where N is the column density [atoms cm^{-2}] and f is the transition oscillator strength (see Spitzer 1978). The equivalent width W_λ measures the fraction of energy removed by the absorption line and is unaffected by the instrumental resolution.

2.—The detailed line-profile fitting method which simulates measured absorption-line spectra by fitting instrumentally blurred multicomponent line profiles to the observed line profiles (e.g., see Spitzer & Morton 1976; Vidal-Madjar et al. 1977).

3.—The continuum reconstruction method which is an important procedure for very strong absorption lines which clearly have Lorentzian damping wings (see Bohlin 1975).

4.—The direct integration of the observed optical depth profile when it seems reasonable to assume that the absorption line is fully resolved, in which case $\tau_a(\lambda) \approx \tau(\lambda)$. This method follows from the connection between optical depth and column density,

$$\tau(\lambda) = \frac{\pi e^2}{m_e c^2} f\lambda^2 N(\lambda) , \quad (7)$$

where $N(\lambda)$ is the column density per unit wavelength and the total column density is given by $N = \int N(\lambda)d\lambda$. If equation (7) is expressed in terms of column density per unit velocity, $N(v)$, the equation becomes

$$\tau(v) = \frac{\pi e^2}{m_e c} f\lambda N(v) = 2.654 \times 10^{-15} f\lambda N(v) , \quad (8)$$

where λ is in angstroms and $N(v)$ is in atoms cm^{-2} (km s^{-1})$^{-1}$. The total column density is given by solving equation (8) for $N(v)$ and integrating

$$N = \int N(v)dv = \frac{m_e c}{\pi e^2 f\lambda} \int \tau(v)dv$$
$$= \frac{m_e c}{\pi e^2 f\lambda} \int \ln \frac{I_0(v)}{I(v)}\, dv . \quad (9)$$

Note that this method makes no a priori assumptions about the functional form of the velocity distribution of the gas unlike the other methods mentioned above. This method has been employed in past studies of the interstellar medium for which high-resolution observations of a single line within a species have been measured. For applications of the technique to optical absorption-line observations, see Hobbs (1971, 1973, 1974, 1978, and references therein) or Stokes (1978).

If measurements exist for two or more absorption lines of a given species differing in the product $f\lambda$, significant empirical information about line saturation and hence $N(v)$ can be inferred directly from the measured apparent optical depth profiles even when using data for which FWHM(line) $\sim$ (0.25–0.50)FWHM(ϕ_I). A number of papers have recently appeared in the literature which exploit this technique (Savage at al. 1989b; Jenkins et al. 1989; Savage, Massa, & Sembach 1990; Joseph & Jenkins 1990; Sembach, Savage, & Massa 1991). However, a detailed discussion of the technique and its range of applicability does not exist. This paper is intended to fill that gap. In § 2 we describe the "apparent optical depth method" and apply it to data for the sight line to HD 64760. In § 3 we use numerical simulations to further illustrate the method and to quantify the errors involved in using it. We demonstrate how these errors depend on the relationship between the real absorption-line widths and the width of the instrumental spread function. We conclude in § 4 by discussing the advantages of the method and those situations for which it is advantageous to use it.

2. THE APPARENT OPTICAL DEPTH METHOD

The apparent optical depth method requires that there be two or more absorption lines of a given species which differ in the product $f\lambda$. The various absorption-line observations are converted into representations of apparent optical depth, $\tau_a(v) = \ln [I_0(v)/I_{\rm obs}(v)]$, and the different measures of $\tau_a(v)$ are then converted into measures of the apparent column density per unit velocity interval, $N_a(v)$, via equation (8) which in logarithmic form is

$$\log [N_a(v)] = \log \tau_a(v) - \log (f\lambda) + 14.576$$
$$[\text{atoms cm}^{-2}\ (\text{km s}^{-1})] . \quad (10)$$

A comparison of the different $N_a(v)$ profiles for the lines differing in $f\lambda$ provides an empirical way of assessing the degree of line saturation present in the true line profiles (i.e., in exp $[-\tau(v)]$). The comparison also yields information about the accuracy to which the derived $N_a(v)$ profiles are valid representations of the true $N(v)$ profile but simply blurred by the instrumental function, $\phi_I(\Delta v)$. The effects of unresolved saturated structure in the true profiles are not large at those velocities where the different $N_a(v)$ profiles are the same or very similar. However, if the $N_a(v)$ profile of the stronger line is significantly smaller than that of the weaker line, the effects of unresolved saturation are important. In those regions of the profiles for which unresolved saturated structure is not significant, a direct integration of the apparent column density profiles,

$$N_a = \int N_a(v)dv , \quad (11)$$

yields valid *instrumentally smeared* column densities over those velocity regions. Note that $N_a \neq N$ for cases in which the line is unresolved unless the integration extends over an entire line for which no saturated structure is present. When applying the technique, one must compare lines with sufficiently different $f\lambda$ in order for the effects of saturation to be observable. A factor of 2 difference in $f\lambda$, applicable to doublet lines, is often adequate, and most of our discussions will involve the application of the technique to doublets.

To illustrate the apparent optical depth technique, we have selected ultraviolet interstellar absorption-line data toward HD 64760 obtained by the *International Ultraviolet Explorer* (*IUE*) satellite. The data were obtained from the *IUE* data archives and are being used in a program to study the highly ionized gas in the ISM being pursued by Edgar & Savage (1991). Doublet lines from various highly ionized species are listed in Table 1. The rest wavelengths and f-values are from Morton & Smith (1973). The absorption lines are well observed in a spectrum produced by averaging data obtained in six *IUE* short-wavelength echelle mode images (SWP 1781, 1797, 4192, 7482, 7717, and 7718). The spectrum has a signal-to-noise ratio of 20 to 30 and a spectral resolution of approximately 20 km s^{-1} (FWHM). For details about the data handling see Edgar & Savage (1991).

The rotational velocity of HD 64760 is large (259 km s^{-1}; Uesugi & Fukuda 1970), allowing interstellar and stellar absorption to be readily separated. Also, the lines of Si IV and C IV occur against the smoothly rising continuum provided by the stellar P-Cygni wind lines of HD 64760. Sample data in the region of the C IV doublet are shown in Figure 1 along with our continuum fit and the uncertainty in that fit. Equivalent widths of the interstellar lines and their $\pm 1\ \sigma$ errors are listed in Table 1. We adopted the procedures of Sembach et al. (1991) in obtaining these measurements and errors.

Logarithmic plots of the apparent optical depth, log $\tau_a(v)$, and the corresponding apparent column density profile, log $N_a(v)$, as a function of velocity are shown as solid lines in Figures 2*a* and 2*b* for the weak and strong interstellar doublet lines of Al III, Si IV, and C IV. When the value of $\tau_a(v)$ is very small and difficult to measure, the inferred values of log $\tau_a(v)$ and log $N_a(v)$ are replaced by crosses. The dots above and below each solid line or cross indicate our assessment of the $\pm 1\ \sigma$ uncertainty in the value of log $\tau_a(v)$ and log $N_a(v)$ introduced by uncertainties associated with continuum placement and statistical errors in the data. The apparent optical depth profiles are converted into the apparent column density profiles through equation (10) and the values of f and λ listed in Table 1.

TABLE 1

EQUIVALENT WIDTHS AND COLUMN DENSITIES TOWARD HD 64760

				COG[a]				$[N_a = \int N_a(v)dv]$[b]			$[N_a{}^c = N_a^{n-1} + \Delta \log N_a^{n-1}]$[c]		
Ion	λ(Å)	f	$W_\lambda \pm 1\,\sigma$ (mÅ)	log N (linear)	log N ($-1\,\sigma$)	log N	log N ($+1\,\sigma$)	log N_a ($-1\,\sigma$)	log N_a	log N_a ($+1\,\sigma$)	log $N_a{}^c$ ($-1\,\sigma$)	log $N_a{}^c$	log $N_a{}^c$ ($-1\,\sigma$)
Al III	1854.720	0.539	263 ± 8	13.20	...	...	...	13.38[d]	13.41[d]	13.44[d]	...	...	...
Al III	1862.795	0.268	204 ± 12	13.39	13.60	13.69	13.82	13.50[d]	13.54[d]	13.58[d]	13.62	13.70	13.81
Si IV	1393.755	0.528	170 ± 6	13.27	...	...	...	13.39	13.42	13.45	...	...	...
Si IV	1402.769	0.262	102 ± 6	13.35	13.38	13.44	13.49	13.38	13.43	13.46	13.38	13.44	13.49
C IV	1548.202	0.194	220 ± 8	13.73	...	...	...	13.85	13.88	13.91	...	...	...
C IV	1550.774	0.097	141 ± 5	13.83	13.92	13.96	14.00	13.89	13.91	13.94	13.89	13.94	13.98

[a] Column densities listed are obtained from a standard curve of growth analysis applied to the listed equivalent widths assuming a simple Doppler broadened line profile. The $\pm 1\,\sigma$ errors are obtained from the listed errors in W_λ and the χ^2 fitting method discussed in Savage, Edgar, & Diplas (1989a). The column marked "linear" contains values of log N based upon the measured equivalent width of the line and the assumption that the line lies on the linear portion of the curve of growth.

[b] Best values and $\pm 1\,\sigma$ upper and lower limits to column densities for each high-ionization absorption line are listed for the various ions. These estimates are based on direct integration of the $N_a(v)$ profiles shown in Fig. 2c. The $\pm 1\,\sigma$ upper and lower limits on N_a include only the uncertainties associated with the statistical fluctuations in the measurements and continuum placement.

[c] Application of the simple column density correction procedure discussed in § 3.3 of the text to the values of log N_a for the doublet lines of Al III, Si IV, and C IV yields the corrected column densities and errors listed; $\Delta \log N_a^{n-1} = \log N_{\rm true} - \log N_a^{n-1}$.

[d] Difference in the log $N_a(v)$ profiles for the two Al III lines (see Fig. 2c) implies that the strong 1854.72 Å line contains unresolved saturated structures. Therefore, the technique for calculating N_a by integrating over the profile provides only a lower limit on N for the strongest line of the doublet. Value obtained for the weaker line at 1862.795 Å will be less affected by this saturation problem but should also be considered a lower limit.

In Figure 2c log $N_a(v)$ for the weaker and stronger components of each doublet are compared. The weak component of the doublet is shown as the solid line, while that for the stronger component is shown as the dotted line. To reduce the complexity in Figure 2c we have not replotted the errors shown as dots in Figures 2a and 2b.

The Al III log $N_a(v)$ profiles shown in Figure 2c reveal the effects of unresolved saturated structures. The values of log $N_a(v)$ for the weaker component of the doublet are larger than those of the stronger component by about 0.2 dex near line center ($v \sim 0$ km s^{-1}). This difference is larger than differences expected from the observational errors (see Figs. 2a and 2b). The numerical simulations of the next section show that such a large discrepancy indicates substantial saturation effects are influencing both components of the Al III doublet near line center.

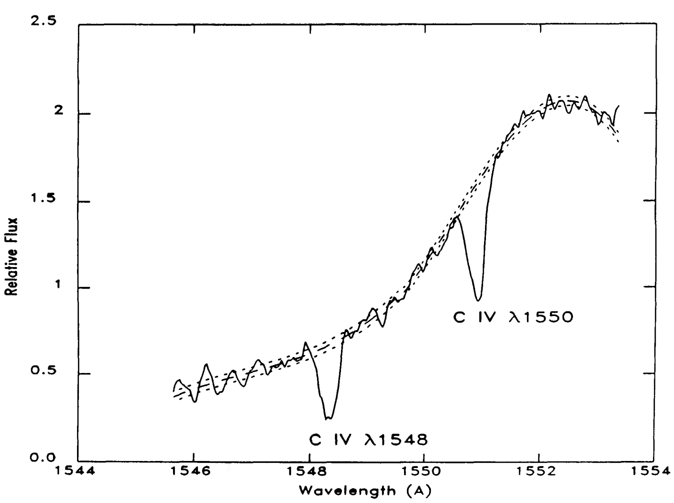

FIG. 1.—Intensity vs. wavelength in angstroms in the vicinity of the interstellar C IV doublet for the B0.5 Ib star HD 64760. The interstellar lines at 1548.202 and 1550.774 Å are positioned on the rising continuum provided by the stellar C IV P-Cygni profile. Spectrum illustrated is an average of six individual *IUE* high-dispersion spectra of HD 64760. The assumed continuum and its $\pm 1\,\sigma$ errors are indicated with the long and short dashed lines, respectively. Absorption-line data like those illustrated here were used to produce the apparent optical depth profiles for highly ionized gas toward HD 64760 shown in Fig. 2.

Because each is saturated, the two Al III log $N_a(v)$ profiles underestimate the true run of column density per unit velocity near line center. However, of the two profiles, the profile for the weaker component of the doublet provides a better instrumentally degraded representation of the true profile. One can see this by comparing the *total* apparent column density of Al III toward HD 64760 derived by integrating the values of $N_a(v)$ over *all* v with total column densities derived by other techniques. Table 1 lists log N_a derived for each component of the various doublets along with $\pm 1\,\sigma$ errors. The value of log N_a for the stronger 1854.720 Å line (13.41) is 0.13 dex smaller than the value (13.54) for the weaker 1862.795 Å line. For these data, the value log N(Al III) = 13.69 obtained from a standard curve of growth analysis applied to the Al III equivalent widths listed in Table 2 is more reliable than either individual total column density derived by a direct integration of the $N_a(v)$ profile. However, an application of the column density correction procedure discussed in § 3.3 to the two values of log N_a results in the estimate log N(Al III) = 13.54 + 0.16 = 13.70, which is consistent with the curve of growth result.

In the case of the values of $N_a(v)$ derived for the doublet lines of Si IV and C IV shown in Figure 2c we note that both components of each doublet have similar $N_a(v)$ profiles. For these two species we can be reasonably confident that the derived log $N_a(v)$ profiles are valid instrumentally degraded representations of the true $N(v)$ profiles. Note that for Si IV and C IV the values of the integrated apparent column density for each component of the doublet agree quite well (see Table 1) and are consistent with the values obtained from a standard curve of growth analysis.

3. NUMERICAL SIMULATIONS

In this section we introduce simulated absorption line profiles and describe how they can be used to understand the effects of unresolved saturated structure in apparent column

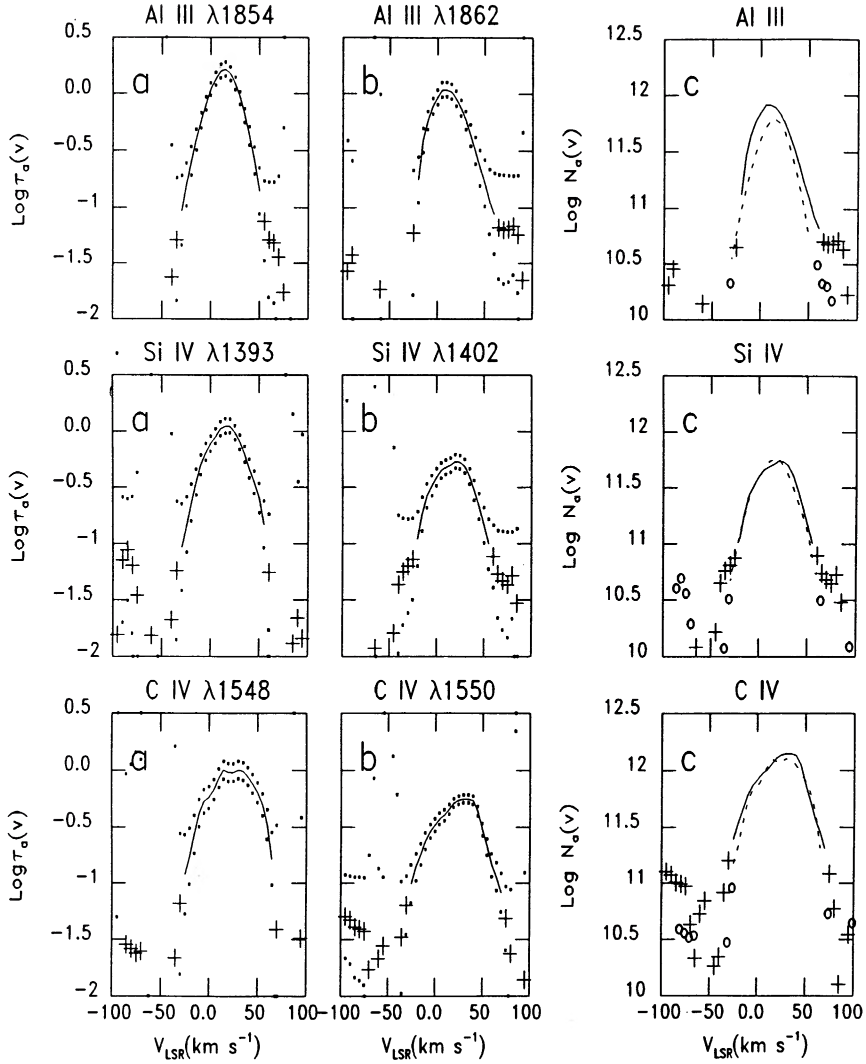

FIG. 2.—(a–b) Logarithmic plots of apparent optical depth $\tau_a(v)$, and apparent column density per unit velocity, $N_a(v)$, vs. LSR velocity for the ultraviolet absorption doublet lines of Al III, Si IV, and C IV are illustrated with the solid lines. Apparent optical depth is defined by eq. (5) in the text while eq. (10) gives the apparent column density profile. When the values of $\tau_a(v)$ are small and difficult to measure, the inferred values are replaced by crosses. Dots above and below each solid line or cross represent our best estimate of the 1 σ errors associated with the combined effects of statistical noise in the data and continuum placement uncertainty. (c) Apparent column density plots from (a) and (b) are illustrated with dashed lines and circles for the stronger line of the doublet (from a) and with solid lines and crosses for the weaker line of the doublet (from b). To reduce the complexity of the plots shown in (c), the dots representing errors from (a) and (b) have not been replotted. When two lines of a doublet produce apparent optical depth profiles that are in good agreement (as for Si IV and C IV) it is unlikely that unresolved saturated structure is strongly influencing the observed profiles. However, unresolved saturated structure is influencing the profiles for Al III. Note that the apparent column density profile for the strong line of Al III in the top panel of (c) (*dashed line*) lies below that for the weak line (*solid line*).

density profiles. In § 3.1 we introduce our approach to simulating data and examine the simple case of an isolated Gaussian component as viewed through instruments having Gaussian spread functions of three different widths. In § 3.2 we simulate a wide variety of situations that may occur for multicomponent absorption lines formed in the interstellar medium. Using these simulations, in § 3.3 we derive an empirical relationship between the true velocity-integrated column density of the absorption and the velocity-integrated column density inferred from the apparent column density profiles containing unresolved saturated structure. We provide a simple saturation correction procedure for obtaining reliable column densities from direct integration of apparent column density profiles. In § 3.4 we compare the results from the apparent optical depth method to those provided by the standard curve of growth method. In § 3.5 we discuss the effects of observational and systematic errors on the derived values of column density obtained through an application of the apparent optical depth method.

3.1. *The Simulation Method and its Application to Single Component Line Profiles*

We construct a set of simulated absorption profiles differing in strength with the following procedure. We assume throughout that the intrinsic absorption lines of individual absorption components, i, in multicomponent profiles have Gaussian shapes characterized by a true optical depth profile,

$$\tau_i(v) = 2^n c_i \exp\left[-(v - v_i)^2/b_i^2\right] , \quad (12)$$

where v_i is the central velocity of the component and b_i (km s^{-1}) = $(2kT/m)^{1/2} = 0.129(T/A)^{1/2}$ is the standard velocity-spread parameter for a species of mass $m = Am_{\rm H}$ at a tem-

TABLE 2

MULTICOMPONENT SIMULATION CHARACTERISTICS

Case	Component (i)	$\langle v_i \rangle$[a] (km s^{-1})	b_i[b] (km s^{-1})	Depth$_i$[c]	W_λ[d] (mÅ)	log N[e]
1.........	1	0	4	0.10	3.666	12.265
2.........	1	0	4	0.10	7.331	12.562
	2	−20	20	0.02		
3.........	1	0	4	0.10	7.331	12.580
	2	−2	4	0.05		
	3	+2	4	0.05		
4.........	1	0	4	0.10	10.996	12.754
	2	−2	4	0.05		
	3	+2	4	0.05		
	4	0	20	0.02		
5.........	1	0	4	0.10	11.912	12.784
	2	−2	4	0.05		
	3	+2	4	0.05		
	4	−10	10	0.01		
	5	−20	20	0.02		
6.........	1	0	4	0.10	13.561	12.836
	2	−10	4	0.05		
	3	−15	4	0.02		
	4	+5	4	0.05		
	5	0	20	0.02		
	6	−10	10	0.02		

[a] Central velocity of the absorption for component i.
[b] Doppler broadening parameter of the absorption for component i.
[c] Central depth, $[1 - \exp(-c_i)]$, of the absorption for component i.
[d] Total equivalent width of the absorption for the case $n = 0$.
[e] Total true column density of the absorption.

perature T (K; see Spitzer 1978). Note that the FWHM of a Gaussian profile is $2(\ln 2)^{1/2}b$. The strength of the feature for component i is determined by the values of $2^n c_i$ where the index, $n = 0$, 1, 2, 3, to 7, allows us to progressively view absorption lines that differ in strength by factors of 2 to simulate the behavior of typical doublet lines of varying strength. The values of c_i, v_i, and b_i are selected to simulate various combinations of strength, central velocity, and width for different types of multicomponent profiles typically encountered along interstellar sight lines. The cases illustrated in this paper are listed in Table 2, where we give the component central depth, $[1 - \exp(-c_i)]$, rather than c_i. The intrinsic optical depth profile, $\tau(v) = \Sigma\tau_i(v)$, for each case was used to compute the true absorption-line profiles, $I(v) = \exp[-\Sigma\tau_i(v)]$, for the strength index, $n = 0$–7. Those profiles were then convolved with various assumed amounts of instrumental smearing according to equation (3) to simulate observed profiles, $I_{\rm obs}(v)$. The instrumental spread functions, $\phi_I(\Delta v)$, were taken to be Gaussian functions with various widths, FWHM(ϕ_I). The simulated observed absorption profiles, $I_{\rm obs}(v)$, were then converted into apparent optical depth profiles, $\tau_a(v)$, and apparent column density profiles, $N_a(v)$, via equations (6) and (10). The column density calculation assumes the absorption for the case where the index $n = 0$ in equation (12) is produced by the resonance line of C IV with $f = 0.097$ and $\lambda = 1550.774$ Å.

To illustrate the method we first consider the simple situation of a single component interstellar line centered at $v = 0$ km s^{-1} with a thermal Doppler broadening parameter, $b = 4$ km s^{-1} (case 1 in Table 2). We illustrate this absorption as the dashed lines in the three panels of Figure 3a, assuming a central depth of 0.1 for the weakest line which has a strength index $n = 0$ (see eq. [12]). In the same figures, we also illustrate the instrumentally smeared versions of this line and lines that are factors of 2, 4, 8, 32, 64, and 128 times stronger for three instrumental spread function widths, FWHM(ϕ_I) = 2.5 km s^{-1} (panel 1), 10.0 km s^{-1} (panel 2), and 40.0 km s^{-1} (panel 3).

The smeared absorption profiles shown in Figure 3a are converted into the aparent optical depth profiles, $\tau_a(v)$, illustrated in logarithmic form in Figure 3b. The intrinsic optical depth profile, $\tau(v)$, for $n = 0$ is illustrated as dashed lines. These apparent optical depth profiles are scaled to produce the apparent column density profiles shown in Figure 3c. The true column density profile, $N(v)$, is illustrated as the dashed line. The equivalent widths for the simulated absorption profiles shown in the three panels of Figure 3a are listed in Table 3. Velocity-integrated apparent column densities, N_a, derived for these lines by direct integration of the simulated profiles are listed in Table 3 for each of the three spread function widths.

We call attention to several important aspects of the apparent column density plots shown in Figure 3c: (1) As the strength of the absorption increases, each apparent column density profile lies lower than one derived for a weaker line, thereby implying that in the absence of observing errors the direct integration of an $N_a(v)$ profile for a strong line yields a lower apparent column density than N_a derived from a weak line. The values of N_a listed in Table 3 confirm this result. (2) The difference between successive $N_a(v)$ profiles increases with increasing line strength. (3) $N_a(v)$ profiles derived from lines differing in strength can disagree at some velocities and agree at others, as is the case for absorption near zero velocity compared to absorption in the wings of the lines (see the 10 km s^{-1} resolution case of the second panel of Fig. 3c). (4) In the case of resolved profiles (i.e., the 2.5 km s^{-1} resolution case shown in the first panel of Fig. 3c) significant departures of the $N_a(v)$ profiles from one another do not occur until the line becomes very strong, whereas in the two unresolved cases sig-

TABLE 3

EQUIVALENT WIDTHS AND COLUMN DENSITIES FOR A SIMPLE ISOLATED GAUSSIAN COMPONENT IN THE ABSENCE OF NOISE[a]

			$N_a = \int N_a(v)dv$[b]		
LINE[c] (n)	f[d]	W_λ[e] (mÅ)	log N_a (2.5 km s^{-1})	log N_a (10 km s^{-1})	log N_a (40 km s^{-1})
0............	0.097	3.668	12.264	12.258	12.252
1............	0.194	7.076	12.263	12.251	12.239
2............	0.388	13.197	12.261	12.236	12.213
3............	0.776	23.145	12.257	12.207	12.163
4............	1.552	36.691	12.248	12.150	12.072
5............	3.104	50.857	12.230	12.046	11.924
6............	6.208	62.474	12.194	11.883	11.722
7............	12.416	71.782	12.117	11.682	11.489

[a] The single Gaussian component has an initial depth of 10% and a thermal Doppler broadening parameter $b = 4$ km s^{-1}. Rest wavelength of the line is 1550.774 Å. True column density for this case is log $N = 12.265$.
[b] Column densities based upon direct velocity integration of the apparent column density profiles shown in Fig. 3c. Values shown are for three different widths of the instrumental spread function, a Gaussian with FWHM = 2.5, 10.0, and 40.0 km s^{-1}.
[c] Line $n = 0$ corresponds to the intrinsic absorption line convolved with the instrumental spread function. Successive lines are factors of 2^n times stronger.
[d] The f-values calculated assuming an f-value of 0.097 for $n = 0$ and a value of $2^n(0.097)$ for $n = 1$–7 (see eq. [12]). Since these numbers are only used to provide the line strength scaling, the fact that some of the values of f are unphysically large has no significance.
[e] Total equivalent width of the absorption.

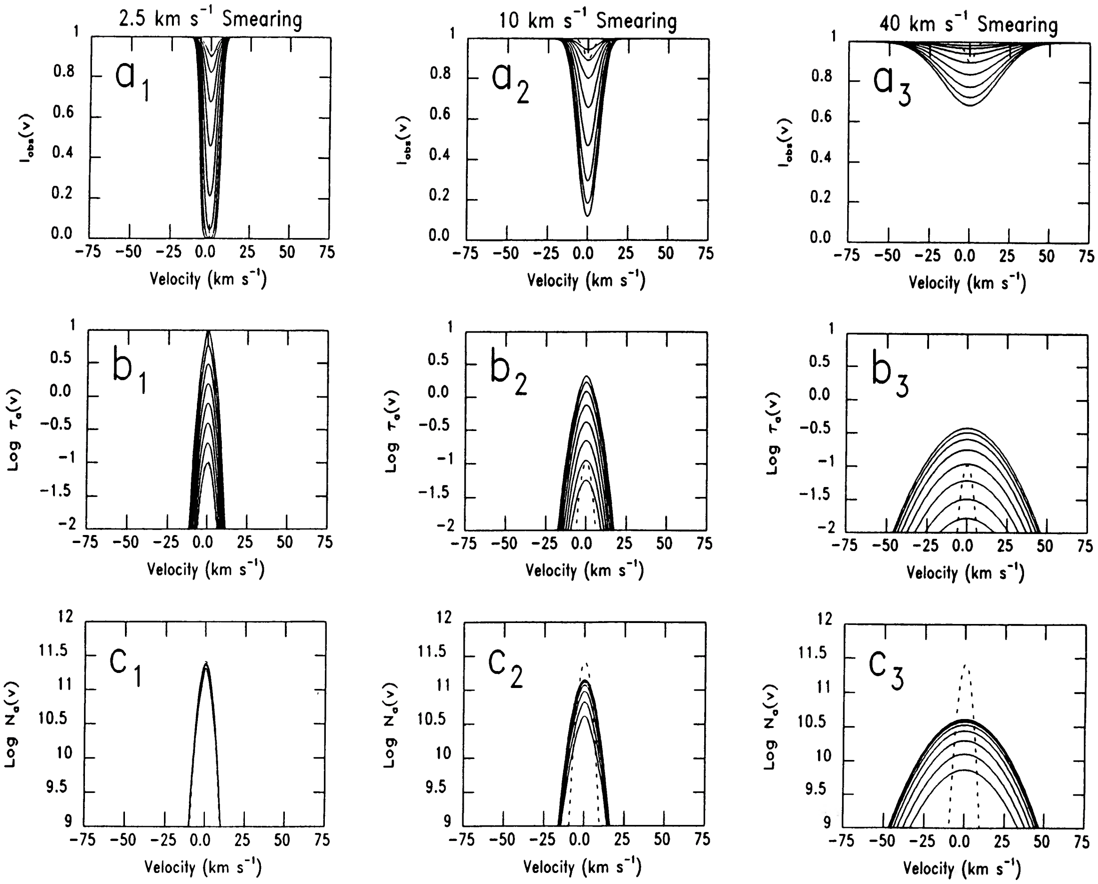

FIG. 3.—Illustrations of simulations of the apparent optical depth method for single component interstellar lines centered at $v = 0$ km s^{-1} with Doppler broadening parameter $b = 4$ km s^{-1}. Three different values of instrumental smearing are assumed for the absorption line profiles shown in the panels in (*a*) (FWHM = 2.5, 10, and 40 km s^{-1}, respectively). In each panel, lines increasing in optical depth by factors of 2, 4, 8, 16, 32, 64, and 128 are shown to simulate how doublet resonance lines which differ in the product $f\lambda$ by a factor of 2 would appear as they grow in strength. In the panels in (*b*) the logarithms of the apparent optical depth profiles, log $\tau_a(v)$, are shown, while in the panels in (*c*) the logarithms of the apparent column density per unit velocity profiles, log $N_a(v)$, are shown. For reference, we illustrate with the dashed lines the appearance of the true line profile for the weakest line (*a*), the true optical depth profile for the weakest line (*b*), and the true column density per unit velocity profile assumed in the simulation (*c*).

nificant departures of the $N_a(v)$ profiles from one another are already evident in lines which are only a few times stronger than the weakest line. These departures indicate that there is strong absorption hidden in the profile as a result of the instrumental smearing. It is this absorption that we refer to as "unresolved saturated structure." For lines that do not show large departures in $N_a(v)$ from one another, the apparent column density profiles provide valid instrumentally degraded representations of the intrinsic $N(v)$ profile. Integration of the $N_a(v)$ profiles in regions where the profiles agree yields reliable instrumentally smeared column densities for these regions according to equation (11). An integration over the entire profile may yield a column density lower than the true column density because of saturation effects in the regions where the profiles do not agree. To quantify how large these departures must be before significant column density information is lost, we turn now to examining simulations of multicomponent lines profiles.

3.2. *Multicomponent Analysis*

We have extended the qualitative analysis of the previous section to examine the relationship between the true column density of the line and the column density one would estimate by direct integration of the $N_a(v)$ profiles. We simulate a variety of multicomponent absorptions that might arise in the ISM, including isolated components, overlapping components, and multiple components of varying widths and strengths. The line profile characteristics of six cases are listed in Table 2.

Note that our choices of b for the narrow components listed in Table 2 correspond to values associated with the warm diffuse interstellar medium. However, all our results can be scaled to other choices of b (either smaller or larger) by noting that the effects of instrumental smearing on the profiles scale with the ratio of b and v for each component to the instrumental smearing width FWHM(ϕ_I). For example, case 2 in Table 2 with components at 0 and -20 km s^{-1} having $b = 4$ and 20 km s^{-1}, when smeared with a Gaussian having FWHM = 20 km s^{-1} would resemble a case with components at 0 and -5 km s^{-1} having $b = 1$ and 5 km s^{-1} when smeared with a Gaussian having FWHM = 5 km s^{-1}.

The intrinsic absorption and its instrumentally smeared version for the six cases are shown in Figures 4*a*–9*a*. A set of lines increasing successively in strength by factors of 2 is also shown for each case in the same figure. The logarithmic apparent optical depth and apparent column density profiles for these cases are shown in Figures 4*b* to 9*b* and in Figures 4*c* to 9*c*, respectively, for an instrumental spread function with FWHM = 20 km s^{-1}, comparable to that of the echelle spec-

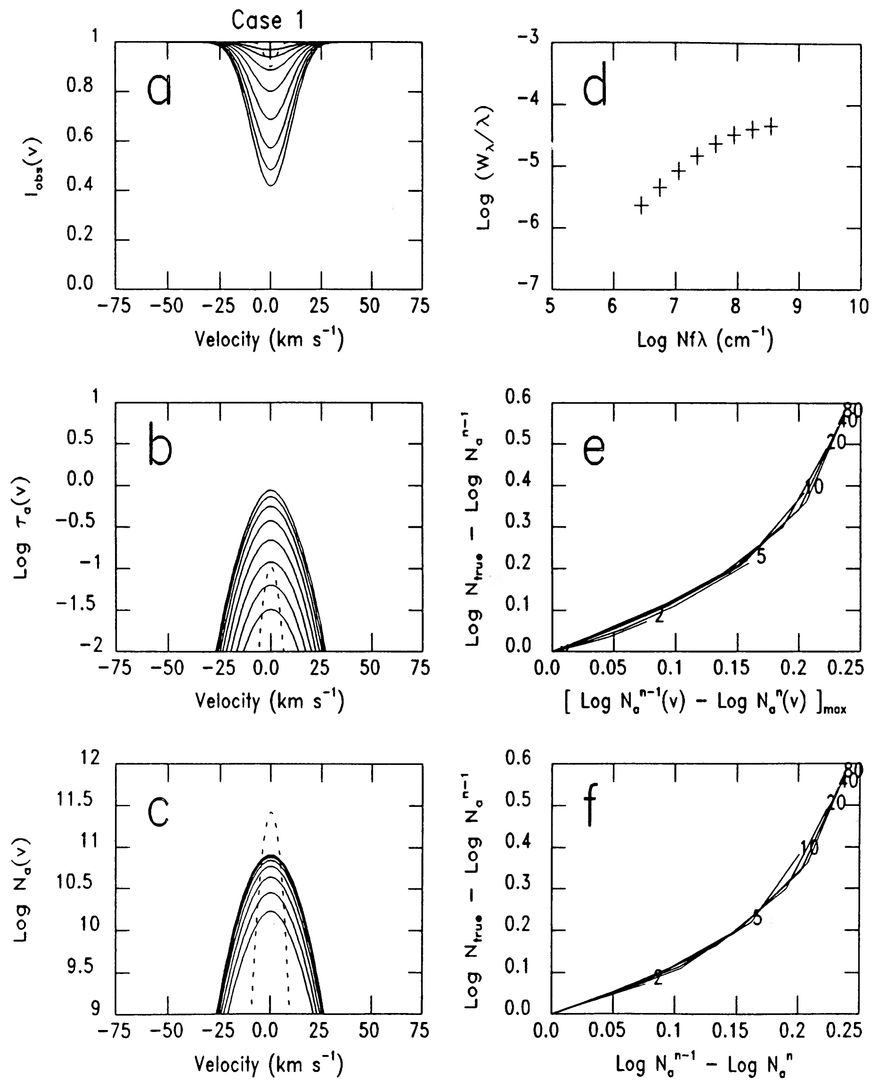

FIG. 4.—(*a–f*) Simulations of the apparent optical depth method for case 1 of Table 2. Panels (*a–c*) show the same form of presentation illustrated in Fig. 2*a*–2*c*. Line profiles shown have been convolved with a Gaussian instrumental smearing function having FWHM(ϕ_I) = 20 km s^{-1}. In (*a–c*) lines increasing in optical depth by factors of 2, 4, 8, 16, 32, 64, and 128 are shown to simulate how doublet resonance lines which differ in the product $f\lambda$ by a factor of 2 would appear as they grow in strength. In (*a*) the absorption profiles for these lines are shown. In (*b*) the logarithm of the apparent optical depth profiles, log $\tau_a(v)$, are shown. In (*c*) the logarithm of the apparent column density per unit velocity profiles, log $N_a(v)$, are shown. For reference, we illustrate with dashed lines the appearance of the true line profile for the weakest line (*a*), the true optical depth profile for the weakest line (*b*), and the true column density per unit velocity profile assumed in the simulation (*c*). Panel (*d*) shows a curve of growth derived from the measured equivalent widths of the absorption profiles shown in (*a*) and the true column density of the absorption listed in Table 2. Note that the lines shown in (*a*) show varying degrees of saturation, ranging from very mildly saturated ($n = 0$) to moderately saturated ($n = 6$). Panel (*e*) shows log N_{true} − log N_a^{n-1} plotted against [log $N_a^{n-1}(v)$ − log $N_a^n(v)$]$_{max}$, where the column densities per unit velocity are evaluated at a velocity where the logarithmic difference is largest. The different curves show this relationship for case 1 and Gaussian smearing functions having FWHM(ϕ_I) = 2.5, 5.0, 10.0, 20.0, 40.0, and 80.0 km s^{-1}. Panel (*f*) shows log N_{true} − log N_a^{n-1} plotted against log N_a^{n-1} − log N_a^n. The different curves show this relationship for case 1 and Gaussian smearing functions having FWHM(ϕ_I) = 2.5, 5.0, 10.0, 20.0, 40.0, and 80.0 km s^{-1}.

trograph aboard the *IUE* satellite. In Figures 4*d* to 9*d* we show a curve of growth derived from the measured equivalent widths of the lines and the true velocity-integrated column densities listed in Table 2.

3.3. *A Column Density Correction Procedure*

Since the apparent optical depth method requires two or more lines, and it is common to work with doublet lines, we have chosen to examine the relationship between the true column density of the absorption, N_{true}, and the apparent column densities, N_a^{n-1} and N_a^n, derived by direct integration of the apparent column density profiles of the weak and strong lines of a doublet. Note that the index n indicates the line strength scaling for the line optical depth according to equation (12). The column density error incurred by integrating the $N_a(v)$ profile of the weaker line in the doublet can be expressed as log N_{true} − log N_a^{n-1}. In Figures 4*e*–9*e* we compare this quantity to

$$[\log N_a^{n-1}(v) - \log N_a^n(v)]_{max} ,$$

the logarithmic difference between the two apparent column density profiles of the doublet at the velocity, v, where that difference is a maximum. Instrumental smearing functions having FWHM(ϕ_I) = 2.5, 5.0, 10.0, 20.0, 40.0, and 80.0 km s^{-1} are assumed for these comparisons to provide a wide range of the ratio of instrumental width to line width. As a general rule,

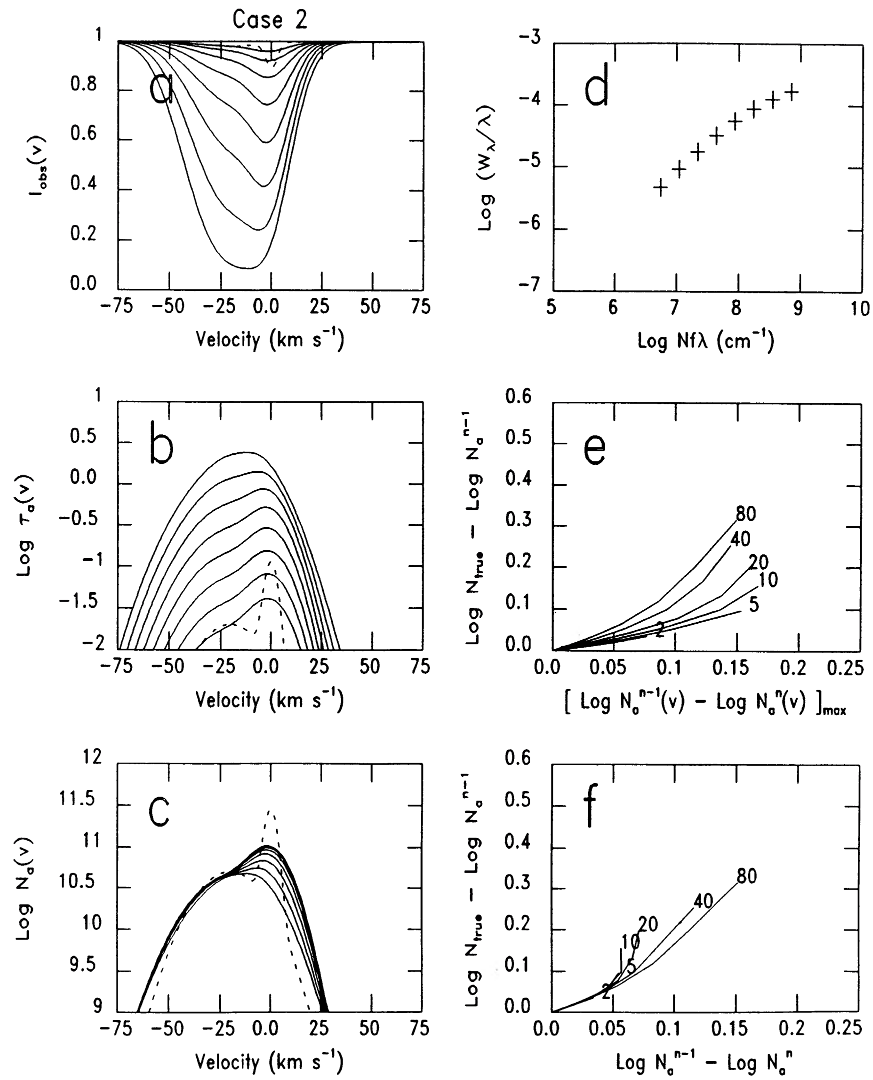

FIG. 5.—Same as for Fig. 4 except for multicomponent case 2 of Table 2

if [log $N_a^{n-1}(v)$ − log $N_a^n(v)]_{max}$ is less than 0.075, the integrated apparent column density inferred from the weaker line of the doublet will be within 0.1 dex (~25%) of the true column density. However, this result is somewhat dependent on the absorption profile shape and instrumental spread function. The range of simulations shown in Figures 4–9 should allow the reader to evaluate the errors likely associated with a particular observational situation.

In Figures 4*f*–9*f* we illustrate the dependence of log N_{true} − log N_a^{n-1} on the logarithmic difference between the two velocity integrated apparent column densities,

$$\log N_a^{n-1} - \log N_a^n ,$$

for the same cases illustrated in Figures 4*e*–9*e*. The difference between the curves shown in Figures 4*e*–9*e* and those shown in Figures 4*f*–9*f* is that instead of assessing the difference between profiles at a particular velocity, we compare the velocity-integrated apparent column densities of the weak and strong line of a doublet, N_a^{n-1} and N_a^n. The "normalization" provided by considering the integrated column densities, as opposed to column density differences at a particular velocity, eliminates some of the spread in Figures 4*e*–9*e* caused by the different instrumental smearing functions. In all of the cases shown, log N_{true} − log N_a^{n-1} is linearly related to log N_a^{n-1} − log N_a^n for values of that latter quantity smaller than about 0.05 dex. For larger values of log N_a^{n-1} − log N_a^n the difference between the true and apparent column densities increases rapidly because of the onset of strong line saturation effects, which is equivalent to the flattening of the curve of growth.

The relatively well-defined relation between log N_{true} − log N_a^{n-1} and log N_a^{n-1} − log N_a^n shown in Figures 4*f*–9*f* for small values of log N_a^{n-1} − log N_a^n suggests that it should be possible to correct for the effects of unresolved saturated structure in the measurements when the saturation is not too great. Letting Δ log N_a^{n-1} = log N_{true} − log N_a^{n-1}, an estimate to log N_{true} is given by

$$\log N_a^c = \log N_a^{n-1} + \Delta \log N_a^{n-1} \qquad (13)$$

with the correction, Δ log N_a^{n-1}, determined from the relationship between log N_{true} − log N_a^{n-1} and log N_a^{n-1} − log N_a^n shown in Figure 4*f* for the simple single component Doppler broadened line. The correction factor, Δ log N_a^{n-1}, is listed in Table 4 as a function of log N_a^{n-1} − log N_a^n.

In Figure 10 we combine the data shown in Figures 4*f*–9*f*.

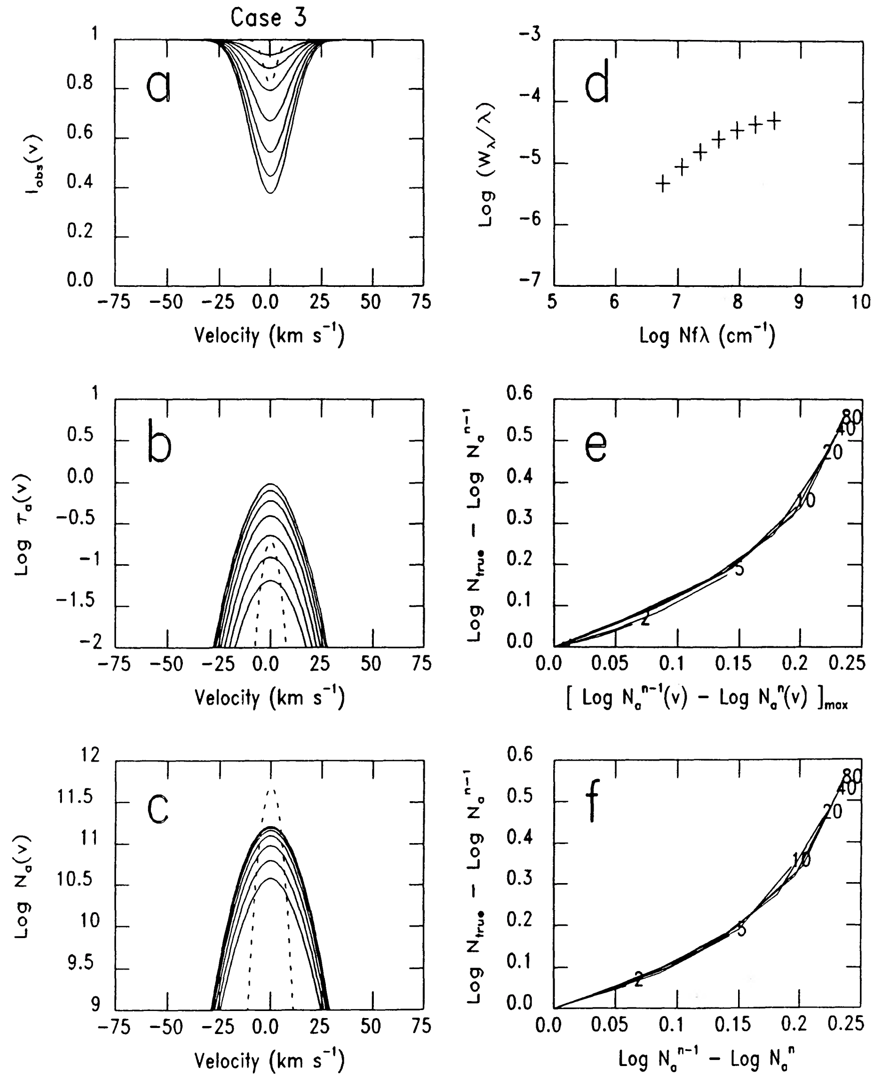

FIG. 6.—Same as for Fig. 4 except for multicomponent case 3 of Table 2

The solid dots represent data in the regime where the relationship between $\log N_{\rm true} - \log N_a^{n-1}$ and $\log {}_a^{n-1} - \log N_a^n$ is well behaved. For $\log N_a^{n-1} - \log N_a^n > 0.05$ dex, the data points are represented by their corresponding multicomponent case number (see Table 2). The errors in column densities corrected by this procedure increase rapidly for $\log N_a^{n-1} - \log N_a^n > 0.05$ dex. For example, for $\log N_a^{n-1} - \log N_a^n$ between 0.06 and 0.10 dex, the errors for specific cases (i.e., cases 2, 4, and 5 involving a narrow and broad component) range from 0.12 to 0.14 dex. However, for all these cases the presence of such large errors is evident in the observed profiles for the two lines of the doublet since the values of $[\log N_a^{n-1}(v) - \log N_a^n(v)]_{\rm max}$ exceed 0.1 dex at the velocities of the narrower components.

Most of the spread in the relationship shown in Figure 10 involves cases in which an unresolved narrow component and a nearly resolved broad component occur. The combination of an unresolved component and a nearly resolved component results in a profile shape that changes dramatically with increasing line strength. This general combination of components has been shown to significantly influence curve of growth analyses as well (Nachman & Hobbs 1973; Jenkins 1986). The cases for which there is no such combination (cases 1 and 3) or for which there is a wider variety of component widths (case 6) are much better behaved to larger values of $\log N_a^{n-1} - \log N_a^n$. The correction factor listed in Table 4 is derived for a single component line profile but may be applied to more complex profiles as well in much the same way that a single component curve of growth analysis is often applied to complex line profiles.

3.4. *Comparison with Curve of Growth*

In this section we compare the results of the apparent optical depth method with those obtained by using a single component Doppler-broadened curve of growth. Such a comparison lends insight into when direct integration of an apparent column density profile provides an adequate measure of the total column density of an interstellar species. These comparisons also show under what physical situations a simple curve of growth analysis might not provide reliable column densities.

In a curve of growth analysis, the equivalent widths of two or more lines differing in the product $f\lambda$ within a species are used to derive integrated column densities by fitting the equivalent widths to a theoretical relation between W_λ/λ and $Nf\lambda$.

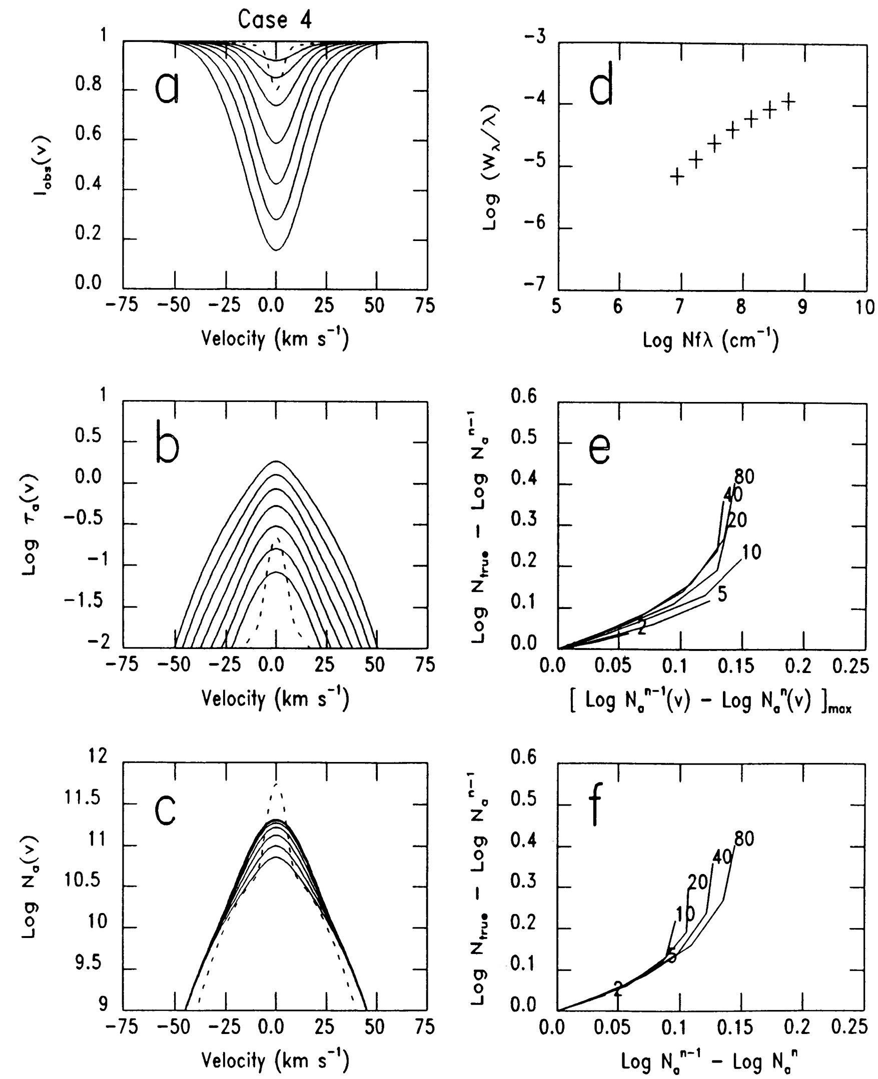

FIG. 7.—Same as for Fig. 4 except for multicomponent case 4 of Table 2

This technique assumes that the functional form of the velocity distribution within the absorbing region can be described as a simple Gaussian distribution (although slightly more complicated forms such as Voigt profiles or multiple Gaussian profiles are used in various situations) with a width characterized by a velocity-spread parameter, *b*, which is allowed to vary in the fitting procedure. A major disadvantage of this technique is that all velocity-dependent information in the absorption profiles is integrated away. The description of the absorption lines is bundled into the measured total equivalent widths of the lines and the fitted value of *b*. Absorption profiles are often much more complicated than single component models and can present serious problems for curve of growth analyses in some cases. For a review of the application of curve of growth analyses to multicomponent sight lines, see Jenkins (1986).

In contrast to the curve of growth technique outlined above, the apparent optical depth method utilizes available velocity information in the profile to provide column densities and saturation information as described in § 2. The apparent optical depth technique makes no assumption about the velocity distribution of the absorbing gas and can be applied to complex sight lines with the same ease that it can be applied to simple sight lines.

The column densities derived from a curve of growth analysis and the apparent optical depth method for the six sight line cases listed in Table 2 are presented in Table 5. For each case, a Gaussian instrumental spread function with FWHM(ϕ_I) = 20 km s^{-1} is assumed, which implies that the instrumental resolution is about 3 times larger than the widths of the narrowest components included in the simulations. The curve of growth column densities are obtained by fitting successive pairs of lines to a single component Doppler-broadened curve of growth. The column densities for the apparent optical depth method are obtained by direct velocity integrations of the weaker line in each line pair. For each case, the maximum true optical depth of the profile is listed for the weaker line in each line pair. Values of log N_a^{n-1} − log N_a^n are also listed in Table 5. The last column included for each case presented in Table 5 lists corrected column densities, log N_a^c, according to equation (13) (see Fig. 10 and Table 4). Percentage errors calculated using the true column densities listed in Table 2 are listed in parentheses after all column densities in Table 5.

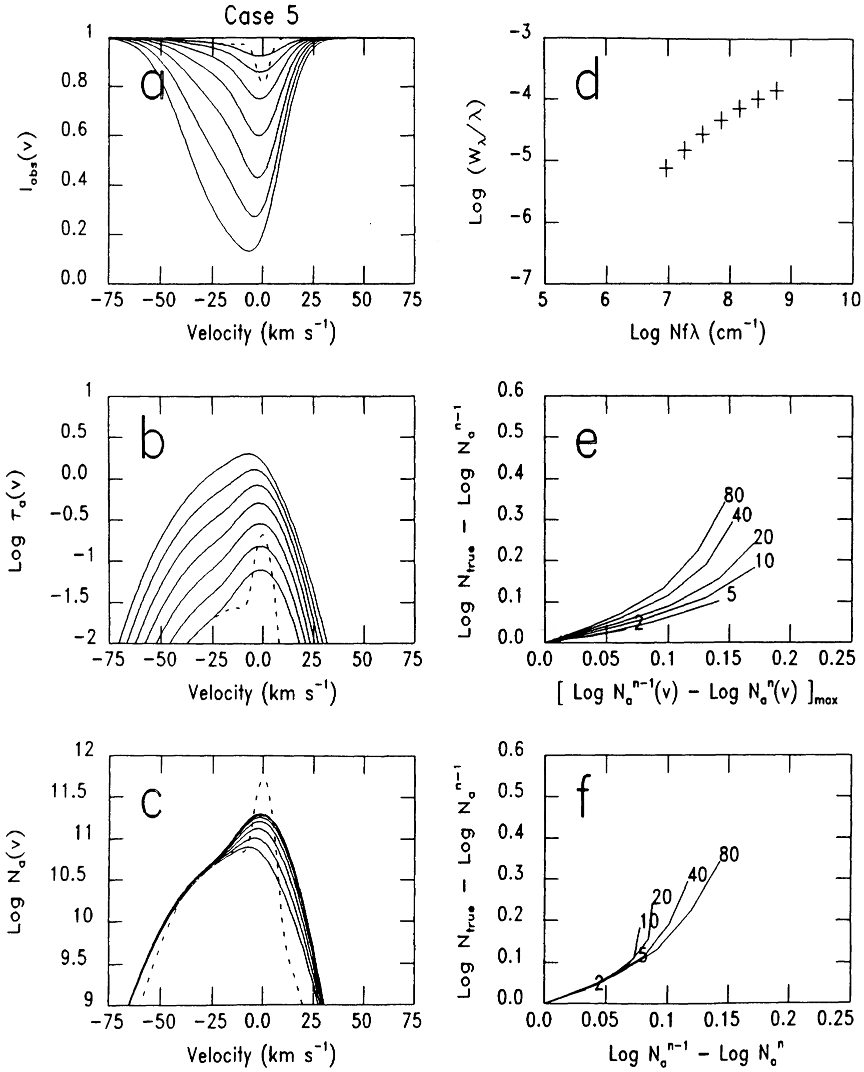

FIG. 8.—Same as for Fig. 4 except for multicomponent case 5 of Table 2

An inspection of the percentage errors given after the various column densities listed in Table 5 leads to the following conclusions: (1) The simple curve of growth analysis gives accurate results (errors $\leq 10\%$) for $\tau^{n-1}(v)_{max} < 2$ for the cases considered. (2) For $\tau^{n-1}(v)_{max} > 2$, the simple curve of growth analysis can introduce large errors in some situations (i.e., cases 4 and 5). (3) For log N_a^{n-1} − log $N_a^n < 0.04$ the values of N_a^{n-1} are accurate to better than 10% as expected from Figure 10 and Table 5. It is clear that when the disparity between intrinsic component line width and the spectroscopic smearing width becomes ≥ 3, one should be cautious about trusting column densities obtained by direct integration of apparent column density profiles. (4) When $\tau^{n-1}(v)_{max}$ exceeds ~ 2, direct integration of the $N_a(v)$ profiles may begin to result in large errors. For these larger values of $\tau^{n-1}(v)$, an application of the simple column density correction procedure outlined in the previous section produces results which are at least as reliable as a simple curve of growth analysis.

For the results listed in Table 5, the instrumental spread function width is a factor of 3 times larger than the narrowest component width. As the ratio of spread function width to narrowest component width decreases, the column density estimate from a direct integration of the $N_a(v)$ profile becomes more reliable. As this ratio approaches 1 (i.e., the line becomes resolvable), the column density estimate quickly approaches the true column density as expected from equations (8) and (9). In or near the resolvable regime, we find that the apparent optical depth method often provides more reliable column densities for multicomponent sight lines than a curve of growth analysis. In fact, the column densities provided by the apparent optical depth method in or near the resolvable regime are often reliable to within $\sim 10\%$ up to true optical depths as large as 8 to 10.

In cases for which only a single line within a species exists, direct integration of the apparent column density profile for the line provides a better lower limit to the true column density than using the equivalent width of the line and the assumption that the line falls on the linear portion of the curve of growth. Table 1 lists the column densities of Al III, Si IV, and C IV obtained toward HD 64760 using the linear approximation to the curve of growth and direct integration of the $N_a(v)$ profiles. For each line, the direct integration of $N_a(v)$ provides a better (larger) lower limit to the true column density than the linear approximation. This result is independent of the width of

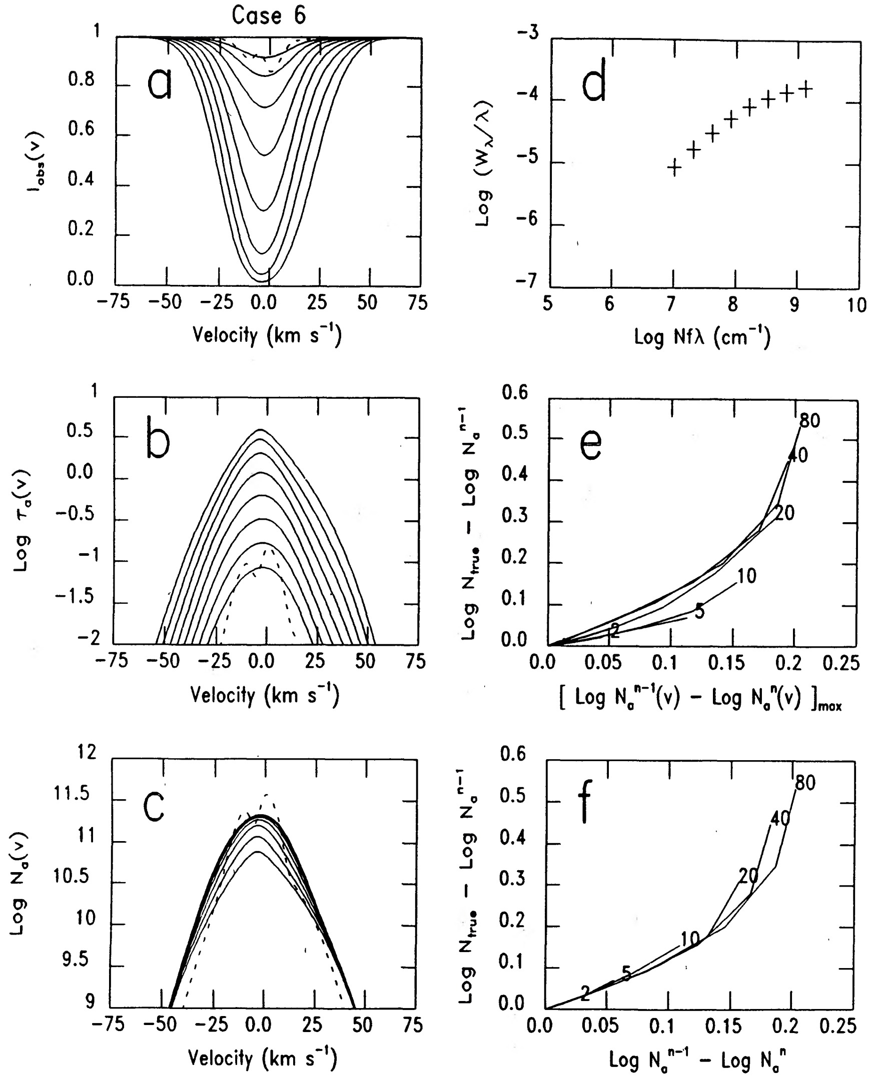

FIG. 9.—Same as for Fig. 4 except for multicomponent case 6 of Table 2

the instrumental smearing function and complexity of the absorption.

As a final comparison of the two methods, we note that it is computationally simpler to obtain column densities and corresponding errors by application of the correction procedure outlined above than by a curve growth analysis. Curve of growth applications require minimization of a function over a two-dimensional surface ($N \times b$). However, the correction procedure presented here requires only estimates of the column densities for a pair of lines (as opposed to equivalent widths for the curve of growth) and a simple interpolation in Table 4. The errors on these individual column density estimates can be propagated through this interpolation as well to produce error estimates in accord with those provided by a careful curve of growth analysis (see Table 1).

3.5. *Observational and Systematic Errors*

With modern detectors it is possible to obtain spectra of interstellar absorption lines with high signal-to-noise ratios. The apparent optical depth method generally requires such data. In § 3.3 we saw that apparent column density profiles for doublet lines that agree to better than approximately 0.05 dex or 12% can have their total column densities very accurately corrected for the presence of unresolved saturated structure. In general, one must be careful in applying the above correction to observed data. The quantity $\log N_a^{n-1} - \log N_a^n$ is very dependent on the measurement errors of the data, especially when the lines become very strong. To apply the correction with reasonable accuracy requires high signal-to-noise ratios for lines such as those listed for HD 64760 in Table 1. However, we strongly emphasize that the usefulness of the apparent optical depth technique lies in its ability to locate unresolved saturated structures within the apparent column density profiles. The ability to detect unresolved saturated structure at a particular velocity depends upon both the measurement errors and the amount of saturation at that velocity. The desired degree of accuracy in derived values of $N_a(v)$ suggest that spectra with $S/N \gtrsim 20$–30 due to photon statistics are often sufficient to detect unresolved saturated structure in the $N_a(v)$ profiles (Fig. 2, Al III data). Errors due to other factors, such as detector fixed pattern noise, can usually be removed with ample precision either through accurate flat-fielding or by obtaining spectra with a number of different

TABLE 4

COLUMN DENSITY CORRECTIONS FOR AN ISOLATED GAUSSIAN COMPONENT

$[\log N_a^{n-1} - \log N_a^n]$[a]	$[\Delta \log N_a^{n-1}]$[b]
0.000	0.000
0.010	0.010
0.020	0.020
0.030	0.030
0.040	0.040
0.050	0.051
0.060	0.061
0.070	0.073
0.080	0.085
0.090	0.097
0.100	0.111
0.110	0.125
0.120	0.140
0.130	0.157
0.140	0.175
0.150	0.195
0.160	0.217
0.170	0.243
0.180	0.273
0.190	0.307
0.200	0.348
0.210	0.396
0.220	0.453
0.230	0.520
0.240	0.600

[a] Difference in velocity-integrated apparent column densities between the weak and strong lines of a doublet.

[b] Column density correction, $\Delta \log N_a^{n-1} = \log N_{\rm true} - \log N_a^{n-1}$, based on linear interpolation of data shown in Fig. 4*f* for an isolated Gaussian component as seen through instruments with various spread function widths. Apparent column density of the weak line in a doublet, N_a^{n-1}, can be corrected to provide a more accurate column density via $\log N_a^c = \log N_a^{n-1} + \Delta \log N_a^{n-1}$.

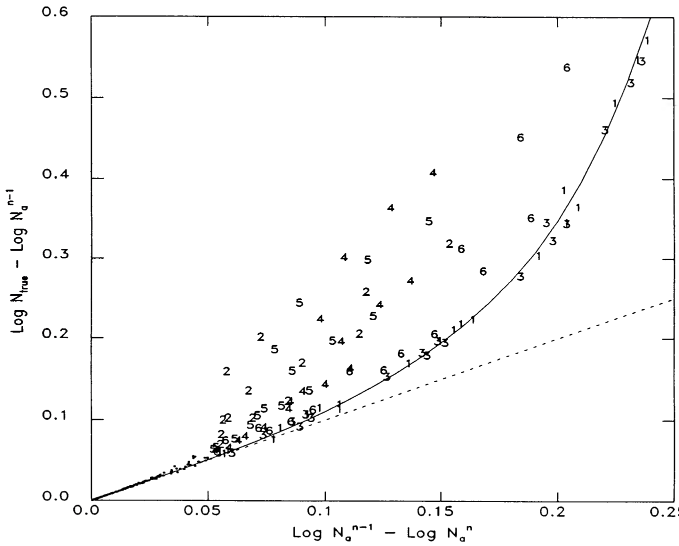

FIG. 10.—$\Delta \log N_a^{n-1} = \log N_{\rm true} - \log N_a^{n-1}$ is plotted against $\log N_a^{n-1} - \log N_a^n$ for all the cases illustrated in Figs. 4*f*–9*f*. Dots represent values in the regime where the relationship between the two quantities for all the cases follow the same curve. Points outside this region are shown by their respective case number. Solid line shows the relationship for a single component Doppler broadened line (case 1). Values for this case can be used to provide a correction to measured values of $\log N_a^{n-1}$ (see Table 4). The dashed line illustrates a 1:1 relation between $\log N_{\rm true} - \log N_a^{n-1}$ and $\log N_a^{n-1} - \log N_a^n$. The figure can be used to estimate errors associated with an application of the apparent column density correction procedure described in § 3.3. For $\log N_a^{n-1} - \log N_a^n > 0.05$, the errors can be large when the absorption involves a combination of narrow and broad components.

wavelength set up positions in order to average over the fixed pattern structure.

Reliable continuum placement also depends on the signal-to-noise ratio of the data and requires background sources with relatively smooth continua. This can be a problem, especially in the ultraviolet, where the spectra of hot stars can be quite complex. Choosing a star with a suitably large rotational velocity, $v \sin i$, can help. However, if the rotation is too great, the possibility of interstellar line contamination from the presence of circumstellar gas can present problems. Also, in some situations hot stars with large rotational velocities exhibit photospheric profile distortions caused by nonradial oscillations (Vogt & Penrod 1983). Note that the methods employed for fitting continua differ among authors (see, e.g., Bohlin et al. 1983; Cardelli et al. 1990; Sembach et al. 1991). Continuum placement errors are particularly important for weak lines.

Accurate background corrections can sometimes be difficult to achieve. The error, σ_δ, in apparent optical depth, $\tau_a(v)$, incurred by a zero-level uncertainty, δ, in a normalized line profile is given by

$$\sigma_\delta[\tau_a(v)] = \ln\{1 + \delta \exp[\tau_a(v)]\} . \tag{14}$$

One can see from the expression that the error due to background uncertainties increases with increasing optical depth per unit velocity. The corresponding error incurred in $N_a(v)$ is found by propagating this error through equations (8) or (10).

Uncertainties in atomic transition probabilities or f-values are another problem. These uncertainties affect all column density estimates and can often be quite large, especially for weak transitions. As a general rule, f-values known to an absolute level of $\pm 15\%$ are considered to be reliable. However, for multiplet lines, relative f-values will normally be better known than absolute f-values, and it is the relative value of $f\lambda$ from one line to the next that plays the largest role in the scaling from apparent optical depth to apparent column density provided through equation (10).

4. DISCUSSION

The value of the optical depth method lies in its ability to reveal the location of unresolved saturated structure in the $N_a(v)$ profiles, and hence in the observed absorption-line profiles. Unlike other techniques, this method makes no a priori assumptions regarding the velocity distribution of the absorbing gas and permits a study of the full velocity dependence of the absorption and how it changes from ion to ion. Depending on the nature of the absorbing medium, the apparent optical depth method may have a number of important advantages over standard curve of growth and detailed profile fitting methods commonly used in the analysis of interstellar absorption lines. We summarize some of these advantages below.

1.—In the apparent optical depth method the data are directly converted into a form [e.g., $N_a(v)$ profiles] that are valuable for scientific interpretations and discussions. This is particularly true in situations where the absorption profile velocity and component characteristics are complex. When

TABLE 5

Apparent Optical Depth—Curve of Growth Comparison (Cases 1–6)[a]

Line pair[e] (n, n-1)	Case 1: Max[f] $\tau^{n-1}(v)$	Case 1: [log N_a^{n-1} - log N_a^{n}]	Case 1: N_a[b] log N_a^{n-1}	Case 1: N_a^c[c] log N_a^c	Case 1: COG[d] log N	Case 2: Max[f] $\tau^{n-1}(v)$	Case 2: [log N_a^{n-1} - log N_a^{n}]	Case 2: N_a[b] log N_a^{n-1}	Case 2: N_a^c[c] log N_a^c	Case 2: COG[d] log N
0 - 1	0.105	0.011	12.254 (2.5)	12.265 (<1)	12.262 (<1)	0.113	0.006	12.556 (1.4)	12.562 (<1)	12.562 (<1)
1 - 2	0.211	0.021	12.243 (4.9)	12.264 (<1)	12.264 (<1)	0.227	0.010	12.550 (2.7)	12.560 (<1)	12.560 (<1)
2 - 3	0.421	0.043	12.222 (9.4)	12.266 (<1)	12.266 (<1)	0.454	0.020	12.540 (4.9)	12.560 (<1)	12.559 (<1)
3 - 4	0.843	0.079	12.179 (18.0)	12.262 (<1)	12.260 (1.1)	0.908	0.036	12.519 (9.4)	12.556 (1.4)	12.553 (2.1)
4 - 5	1.686	0.134	12.100 (31.6)	12.267 (<1)	12.269 (<1)	1.817	0.054	12.484 (16.4)	12.539 (5.2)	12.541 (4.7)
5 - 6	3.372	0.191	11.965 (49.9)	12.266 (<1)	12.265 (<1)	3.634	0.066	12.430 (26.2)	12.498 (13.7)	12.495 (14.3)
6 - 7	6.743	0.223	11.775 (67.6)	12.248 (3.8)	12.260 (1.1)	7.268	0.071	12.364 (36.6)	12.438 (24.8)	12.432 (25.9)

Line pair[e] (n, n-1)	Case 3: Max[f] $\tau^{n-1}(v)$	Case 3: [log N_a^{n-1} - log N_a^{n}]	Case 3: N_a[b] log N_a^{n-1}	Case 3: N_a^c[c] log N_a^c	Case 3: COG[d] log N	Case 4: Max[f] $\tau^{n-1}(v)$	Case 4: [log N_a^{n-1} - log N_a^{n}]	Case 4: N_a[b] log N_a^{n-1}	Case 4: N_a^c[c] log N_a^c	Case 4: COG[d] log N
0 - 1	0.196	0.019	12.560 (4.4)	12.579 (<1)	12.580 (<1)	0.220	0.014	12.738 (3.6)	12.752 (<1)	12.756 (<1)
1 - 2	0.391	0.038	12.541 (8.6)	12.579 (<1)	12.579 (<1)	0.441	0.029	12.724 (6.7)	12.753 (<1)	12.753 (<1)
2 - 3	0.783	0.072	12.503 (16.2)	12.578 (<1)	12.577 (<1)	0.882	0.051	12.695 (12.7)	12.747 (1.6)	12.745 (2.1)
3 - 4	1.567	0.125	12.431 (29.0)	12.579 (<1)	12.574 (1.4)	1.764	0.083	12.644 (22.4)	12.732 (4.9)	12.718 (8.0)
4 - 5	3.134	0.182	12.306 (46.8)	12.586 (1.4)	12.568 (2.8)	3.528	0.105	12.561 (35.9)	12.679 (15.9)	12.647 (21.8)
5 - 6	6.268	0.219	12.124 (65.0)	12.571 (2.1)	12.557 (4.9)	7.056	0.107	12.456 (49.6)	12.577 (33.5)	12.530 (40.3)
6 - 7	12.536	...	11.905 (78.9)	...	12.550 (6.7)	14.112	...	12.349 (60.6)	...	12.417 (54.0)

Line pair[e] (n, n-1)	Case 5: Max[f] $\tau^{n-1}(v)$	Case 5: [log N_a^{n-1} - log N_a^{n}]	Case 5: N_a[b] log N_a^{n-1}	Case 5: N_a^c[c] log N_a^c	Case 5: COG[d] log N	Case 6: Max[f] $\tau^{n-1}(v)$	Case 6: [log N_a^{n-1} - log N_a^{n}]	Case 6: N_a[b] log N_a^{n-1}	Case 6: N_a^c[c] log N_a^c	Case 6: COG[d] log N
0 - 1	0.209	0.012	12.772 (2.8)	12.784 (<1)	12.781 (<1)	0.094	0.006	12.830 (1.4)	12.836 (<1)	12.831 (1.1)
1 - 2	0.419	0.023	12.760 (5.4)	12.783 (<1)	12.783 (<1)	0.188	0.012	12.824 (2.7)	12.836 (<1)	12.838 (<1)
2 - 3	0.838	0.042	12.737 (10.3)	12.779 (1.1)	12.780 (<1)	0.377	0.023	12.812 (5.4)	12.835 (<1)	12.838 (<1)
3 - 4	1.675	0.066	12.695 (18.5)	12.763 (4.7)	12.756 (6.2)	0.755	0.046	12.789 (10.3)	12.835 (<1)	12.833 (<1)
4 - 5	3.350	0.085	12.629 (30.0)	12.720 (13.7)	12.698 (18.0)	1.510	0.084	12.743 (19.3)	12.833 (<1)	12.818 (4.1)
5 - 6	6.700	0.087	12.544 (42.4)	12.642 (28.7)	12.621 (31.3)	3.020	0.131	12.659 (33.5)	12.817 (4.3)	12.764 (15.7)
6 - 7	13.400	...	12.457 (52.9)	...	12.559 (40.4)	6.039	0.157	12.528 (50.8)	12.739 (20.0)	12.653 (34.7)

[a] Apparent optical depth–curve of growth column density comparison for the six cases listed in Table 2, assuming a Gaussian instrumental spread function with FWHM(ϕ_I) = 20 km s^{-1}. Percentage errors are listed in parentheses following each column density and are defined by % error = 100 × {[$N_{\rm true}$ − N(calculated)]/$N_{\rm true}$}. Log $N_{\rm true}$ = 12.265, 12.562, 12.580, 12.754, 12.784, and 12.836 for Cases 1, 2, 3, 4, 5, and 6, respectively.

[b] Apparent column density derived from direct integration of the apparent column density profile for line $n - 1$ in each pair.

[c] Corrected apparent column derived by applying the column density correction procedure described in § 3.3 to the pair of lines ($n - 1$, n).

[d] Column density derived from a single component Doppler-broadened curve of growth fit to the pair of lines ($n - 1$, n).

[e] Pair of lines used to compute the curve of growth and corrected apparent column densities. Within each pair, line n is a factor of 2 stronger than line $n - 1$. The strength index, n, is defined in eq. (12) of the text.

[f] Maximum true optical depth of the profile for the weaker line ($n - 1$) in each pair.

inspecting $N_a(v)$ profiles, a reader can often identify the occurrence of physically important phenomena which are easily missed when viewing large tables of numbers which list column densities, velocities, and velocity-spread parameters based on the analysis of individual kinematical components.

2.—The apparent optical depth method provides significant empirical information about the velocity dependence of line saturation. With this technique, an instrumentally degraded version of $N(v)$ can be inferred directly from the measured apparent optical depth profiles even when using data for which FWHM(line) ~ (0.25–0.50) FWHM(ϕ_I). The curve of growth method offers information regarding line saturation based on integrated line quantities but offers no insight into the velocity dependence of the saturation.

3.—Once errors due to unresolved saturated structures are understood, it is possible to directly compare $N_a(v)$ profiles among different interstellar species in order to study the changing physical conditions from one absorption component to another. This technique also allows a wide range of science to be done on broad absorption lines which are very strong but have unsaturated absorption wings produced by intermediate- or high-velocity interstellar gas.

4.—There are many situations involving multiple component absorption where a standard curve of growth analysis or a detailed multicomponent fitting procedure are not particularly tractable because of the kinematical complexity of the sight line. In some of these situations, an application of the apparent optical depth method proceeds quite easily.

5.—In cases where many absorption lines for a given species exist, a complete interstellar column density profile spanning several decades in $N_a(v)$ can be constructed by combining $N_a(v)$ profiles for weak and strong lines. An example of this type of construction applied to interstellar Fe II can be found in Figure 5*e* of Savage et al. (1990).

6.—In cases where only a single absorption line exists, a direct integration of $N_a(v)$ over velocity provides a better (larger) lower limit to the column density of the absorbing species than a simple equivalent width measurement combined with the assumption that the line is on the linear part of the curve of growth.

7.—In cases where saturation exists within the absorption profile, an application of the column density correction procedure described in § 3.3 yields column densities and error estimates *at least* as reliable as those given by a simple curve of growth analysis. We also note that it is computationally simple to derive column densities and error estimates with this procedure.

We note that our interest in the apparent optical depth technique was sparked through a collaboration of one of us (B. D. S.) with Edward Jenkins, Charles Joseph, and Klaas de Boer involving the sight line to SN 1987A (see Savage et al. 1989b). All of the computing required for this investigation was performed at the Midwest Astronomical Data Reduction and Analysis Facility in Madison. We acknowledge many valuable discussions of various aspects of the apparent optical depth technique with Edward Jenkins, Jason Cardelli, and Richard Edgar. Support for this research has been provided through NASA grant NAG-186 and NASA contract NAS 5-29638.

REFERENCES

Bohlin, R. C. 1975, ApJ, 200, 402
Bohlin, R. C., Hill, J. K., Jenkins, E. B., Savage, B. D., Snow, T. P., Spitzer, L., & York, D. G. 1983, ApJS, 51, 277
Cardelli, J. A., Suntzeff, N. B., Edgar, R. J., & Savage, B. D. 1990, ApJ, 362, 551
Edgar, R. J., & Savage, B. D. 1991, in preparation
Hobbs, L. M. 1971, ApJ, 170, L85
———. 1973, ApJ, 180, L79
———. 1974, ApJ, 191, 381
———. 1978, ApJS, 38, 129
Jenkins, E. B. 1986, ApJ, 304, 739
Jenkins, E. B., Lees, J. A., van Dishoeck, E. F., & Wilcots, E. M. 1989, ApJ, 344, 785
Joseph, C. L., & Jenkins, E. B. 1990, ApJ, 368, 201
Morton, D. C., & Smith, W. H. 1973, ApJS, 26, 333
Nachman, P., & Hobbs, L. M. 1973, ApJ, 273, 450
Savage, B. D., Edgar, R. J., & Diplas, A. 1989a, ApJ, 361, 107
Savage, B. D., Jenkins, E. B., Joseph, C. L., & de Boer, K. S. 1989b, ApJ, 345, 395
Savage, B. D., Massa, D., & Sembach, K. 1990, ApJ, 355, 114
Sembach, K. R., Savage, B. D., & Massa, D. 1991, ApJ, 372, 81
Spitzer, L. 1978, Physical Processes in the Interstellar Medium (New York: John Wiley), 51
Spitzer, L., & Morton, W. A. 1976, ApJ, 204, 731
Stokes, G. M. 1978, ApJS, 36, 115
Uesugi, A., & Fukuda, I. 1970, Contr. Inst. Ap. Kawasan Obs., University of Kyoto, No. 189
Vidal-Madjar, A., Laurent, C., Bonnet, R. M., & York, D. G. 1977, ApJ, 211, 91
Vogt, S. S., & Penrod, G. D. 1983, ApJ, 275, 661